Experimental Phase-Space Tomography of Semiconductor Laser Dynamics

D. Brunner,* M. C. Soriano, X. Porte, and I. Fischer
Instituto de Física Interdisciplinar y Sistemas Complejos, IFISC (UIB-CSIC), Campus Universitat de les Illes Balears, E-07122 Palma de Mallorca, Spain

(Received 14 November 2014; published 28 July 2015)

We perform phase-space tomography of semiconductor laser dynamics by simultaneous experimental determination of optical intensity, frequency, and population inversion with high temporal resolution. We apply this technique to a laser with delayed feedback, serving as prominent example for high-dimensional chaotic dynamics and as model system for fundamental investigations of complex systems. Our approach allows us to explore so far unidentified trajectories in phase space and identify the underlying physical mechanism.

DOI: 10.1103/PhysRevLett.115.053901 PACS numbers: 42.55.Px, 05.45.Jn, 42.60.Mi, 42.65.Sf

Shortly after the initial demonstration of semiconductor lasers in the 1960s, it was discovered that these devices are extremely sensitive to time-delayed back reflections of their own emission [1]: in a range from very weak (40 dB attenuated) to strong delayed feedback, one can observe dramatic modifications of their dynamical behavior [2]. While initially the resulting dynamics was mainly considered to be a major nuisance, soon, fundamental aspects of the observed behavior received increasing interest [3]. Delayed-feedback semiconductor lasers became a prime test bed for the scientific study of nonlinear and high-dimensional systems exhibiting chaotic behavior. The dramatic modification to the laser's properties manifests itself in the collapse of the laser's coherence, with an increase of the optical emission linewidth from ~MHz to easily tens of GHz [4]. This reduction of coherence by up to 5 orders of magnitude is accompanied by corresponding picosecond intensity pulsations [5]. As such, the impact of delayed feedback has to be considered as nontrivial.

The state of a free running, single mode semiconductor laser diode biased above threshold is characterized by its carrier inversion (N_0), frequency (ν_0), and intensity (I_0). This solitary laser mode (SLM) usually is a stable fixed point. Delayed feedback strongly modifies the laser's phase-space structure, resulting in a large variety of delay-induced complex phenomena, including narrow linewidth emission or dynamics in the form of limit cycles, quasiperiodic behavior, and deterministic chaos [6,7]. Each of these regimes is characterized by its corresponding phase-space trajectory [8]. Full-bandwidth and realtime measurements of feedback laser intensity [$I(t)$] [5] and frequency [$\nu(t)$] [9] dynamics already revealed significant new insight; however, this lacked the additional information on the carrier dynamics. Though highly successful, reconstructing complete phase space trajectories from scalar or few-variable via Takens' approach does not allow for the association of different phase-space directions to variables of the physical system [10]. Therefore, it is difficult to identify physical mechanisms from such a reconstructed phase space.

Here, we report on the simultaneous experimental determination of the three aforementioned physical phase-space variables with high temporal resolution. Our phase-space tomography therefore allows us to experimentally determine phase-space trajectories, crucial for the correct identification of the laser's dynamical state. Except for an injection locked laser experiment [11], simulations of the semiconductor laser carrier [12,13] and frequency [14] dynamics had to be compared with highly averaged experimental data. Our approach allows for the extraction of physically interpretable information even for single events, something which can be crucial in dynamic and, in particular, chaotic systems. Applying our method to characteristic complex delay-laser dynamics, we identify trajectories of a so far unidentified state, fragmenting the delay interval into two or more clusters. Based on this phase-space tomography, we are able to determine the physical mechanism underlying this dynamical state, demonstrating the opportunities that our method creates.

Our experimental setup is schematically illustrated in Fig. 1. An openly mounted, single mode distributed feedback laser diode ($\lambda_0 \approx 1543$ nm), biased to 7.75 mA ($I_{\mathrm{bias}} = 1.04 I_{\mathrm{th}}$) and operated at 22 °C, has been employed. Laser emission is collected by a single mode optical fiber (SMF-28) with a collection efficiency of ~70%. Using an optical circulator, we form a fiber-based delay loop, in which an optical attenuator and polarization controller are used to accurately define the feedback conditions. Ten percent of the collected emission is outcoupled for detection by a 90/10 optical splitter and amplified by a semiconductor-optical amplifier (gain = 10.2 dB). Combining collection efficiency, attenuations inside the delay loop and outcoupling losses, we obtain a feedback attenuation of ~9 dB. The feedback delay has been determined to be $\tau = 77.6$ ns.

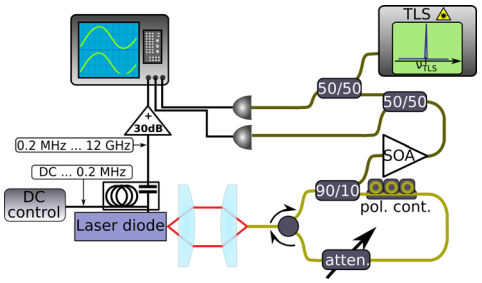

FIG. 1 (color online). Schematic illustration of the experimental setup. A fiber-loop mirror, formed by an optical circulator, forms the delay line ($\tau = 77.6$ ns). The intensity dynamics is directly recorded by a fast detector. Frequency dynamics is reconstructed from a heterodyne time trace, resulting from the interference between the delay laser and a reference source (TLS) [9]. The laser's forward bias is split into dc and rf components; amplification of the rf component by 30 dB allows for its time-resolved detection. All data are simultaneously recorded with a sampling rate of 40 GSamples/s.

The three physical phase-space dimensions of the laser are measured as follows. After amplification by the semiconductor-optical amplifier, the optical signal is split via a 50/50 splitter. At one port intensity dynamics is detected by a fast photodiode. The other port is used for detection of the delay laser's frequency dynamics based on a heterodyne detection scheme [15]: using an additional 50/50 splitter, the delay laser's emission is mixed with a narrow linewidth tunable laser source (TLS). The TLS serves as a reference tuned to a frequency of $\nu_0 = \nu_{\mathrm{TLS}} - 1.8$ GHz. Following [9], using fast Fourier transformation we extract the optical spectrum of the laser within the sliding transformation time interval $\Delta s = (\tau/20)$, defining the laser's optical frequency as the spectral center of mass [15]. Both, intensity and heterodyne signals are detected using fast photo detectors with 20 GHz bandwidth. For carrier dynamics measurements, the laser is electrically connected to a bias tee. The bias tee's low frequency port (dc–0.2 MHz) is used for biasing the laser by a dc current source. The bandwidth of semiconductor laser carrier dynamics typically ranges from ~MHz to ~10 GHz. It can therefore be extracted from the bias tee's radio-frequency port (0.2 MHz–12 GHz), where it is electrically amplified (gain = 30 dB). The detected signal, corresponding to dynamics of the forward bias, is normalized to the dc bias (dV/V_0, $V_0 = 0.8$ V). Not too far above threshold and for the typically small dV, one can approximate the laser's junction capacity to be constant [17]; therefore, $(dV/V_0) \propto (dN/N_0) := \tilde{N}$ [15]. All data are recorded simultaneously using a 40 GSamples/s digital realtime oscilloscope with 16 GHz analog bandwidth.

We demonstrate our phase-space tomography on the complex trajectories of a paradigmatic dynamical state, namely, low frequency fluctuations (LFFs) [14,18–20], a state exhibiting dynamics over multiple time scales. Globally, LFFs are characterized by slow envelope dynamics in all three physical phase-space dimensions. Figure 2(a) depicts experimental full-bandwidth data in the three physical phase-space dimensions, $I(t)$, $\tilde{N}(t)$, and $\nu(t)$, of LFF dynamics. At $t = 0$ one can recognize a sudden drop in intensity, a so-called dropout, associated with a transition towards the SLM and an increased $\tilde{N}$. Subsequently, one observes an increasing average intensity together with an increase in detuning and decrease in $\tilde{N}$. At the end of the cycle, the laser resides in a position of reduced $\tilde{N}$, corresponding to a region of high gain (HGR). External-cavity modes, separated in frequency by τ^{-1}, located between the SLM and HGR, act as a skeleton for this slow time scale dynamics. Under these experimental conditions, the slow SLM-HGR drift requires about ten delays, setting the slowest time scale to $\sim 1\ \mu$s. Representing the intermediate time scale, the delay time τ itself imposes a characteristic time scale on the dynamics. The fast time scales correspond to picosecond intensity pulsations, resulting in hundreds of optical pulses within each τ.

Corresponding phase-space tomography is shown in Fig. 2(b), showing the 3D trajectory in black and its 2D projections in blue shades. We apply a sliding-window averaging filter (160 samples $\triangleq$250 MHz), aiding the interpretation of global phase-space trajectories by

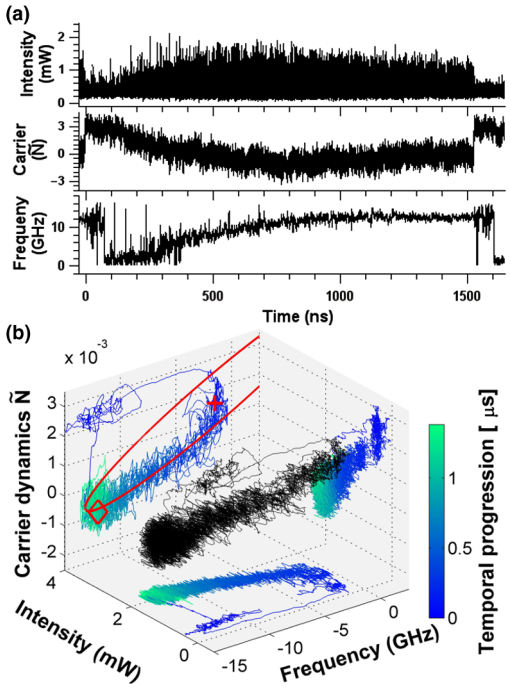

FIG. 2 (color online). Phase-space tomography of a conventional intensity dropout in the LFF regime. Panel (a) shows the full-bandwidth time traces. Panel (b) combines all three physical dimensions to one phase-space plot after applying a 250 MHz low-pass filter. The 3D trajectory is represented in black; the 2D projections include color-coded temporal information. The red (cross) and (diamond) indicate the SLM position and center of the HGR in the $(\tilde{N}, \nu)$ plane; the red line corresponds to the fitted mode ellipse.

reducing the impact of the fast chaotic pulsations [5]. We remain in the $(\tilde{N},\nu)$ plane during the description of LFF phase-space trajectories. Subjected to delayed feedback, the SLM (N_0, ν_0, I_0) is replaced by a large set of external-cavity modes located on a tilted ellipse when projected onto the $(\tilde{N},\nu)$ plane [15,21]. Its eccentricity is determined by α, the laser's amplitude-phase coupling or linewidth-enhancement factor. We fit the ellipse of the external-cavity modes [21] to our experimental trajectory (red line), assuming that the dynamical trajectories are centered around the unstable fixed points. This provides guidance for the interpretation of the global dynamics, additionally indicating the position of SLM (+) and HGR ($\diamond$). We extract the linewidth enhancement factor $\alpha = 2.4 \pm 0.1$ from the ellipse, which is in good agreement with the values reported before for the same device [22].

The $(\tilde{N}, \nu)$ trajectory in Fig. 2(b) starts (deep-blue color) inside the HGR, from where the system is ejected towards the phase-space position of the SLM [23,24]. Once there, the laser slowly drifts towards the HGR along the lower half of the mode ellipse. Superimposed onto the slow drift, one can identify the signatures of the low-pass filtered fast intensity pulsations. Upon approaching the HGR, the drift slows down significantly. The picosecond intensity pulsations continuously induce $\tilde{N}$ perturbations which in turn modify frequency ν due to amplitude-phase coupling (α parameter). Within the HGR this carrier dynamics starts to reach the upper half of the mode ellipse, where destructive interference between the local and delayed-feedback field induces a collapse of the optical field inside the laser, resulting in a crises-induced dropout event. After such an ejection towards the SLM, the LFF cycle restarts [19].

Thus, we have been taking profit of the additional access to physical phase-space dimensions, showing the well-known LFFs in a new light. In the following, we moreover provide experimental evidence for a significant modification to the LFF cycles. In Fig. 3(a), we show full-bandwidth intensity time traces of the conventional LFF of Fig. 2 (upper trace, offset for clarity), and a LFF (lower trace) experiencing τ-periodic fragmentations, a so far undifferentiated and unexplained manifestation of LFF phase-space trajectories. The dynamics of the lower trace of Fig. 3(a) shows fragments of large amplitude pulsations (black data) alternating with time windows of smaller amplitude dynamics (colored data), the duration of two consecutive fragments adding up to approximately τ. This fragmentation does not correspond to the stair or steplike intensity increase obtained by the iterative solution of the Lang-Kobayashi equations found in single [24,25] as well as in coupled lasers [26]. The latter mechanism of which can only explain fragments with single or multiple τ durations, since the τ-iterative solutions results in a homogeneously distributed dynamical state for the entire delay. Dynamical division of one delay into multiple fragments means that the dynamical properties of the delay network are equally

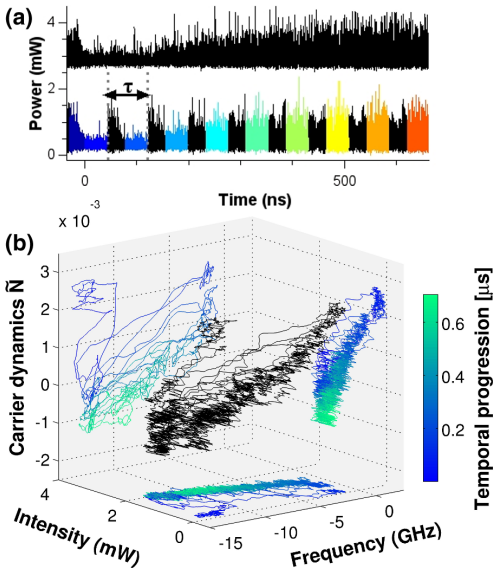

FIG. 3 (color online). (a) Full bandwidth intensity time traces for conventional and fragmented LFFs. Colors of the lower trace highlight the temporal fragmentation. The fragmented LFF's phase-space trajectory is shown in (b). A 250 MHz moving average filter was applied; temporal information is color coded.

grouped into two communities. Strikingly, data of this fragmented LFF as well as data of the conventional LFF of Fig. 2 are both taken from a single recorded experimental time trace; hence, device parameters and operational conditions are identical for both LFF cycles. Similar features were recently reported for semiconductor ring lasers, however not identifying the underlying mechanism [27]. The origin of this dynamical phenomenon remains ambiguous when looking at intensity time traces only.

It is apparent that underlying the τ-periodic intensity pulsations resides more complex behavior. In Fig. 3(b) we show the corresponding trajectory in the three-dimensional physical phase space. The clear modification to the phase space can be appreciated when comparing panels (b) of Fig. 3 and Fig. 2. The laser's fragmented intensity pulsations are the consequence of fast alternations going back-and-forth between the SLM region and the HGR, exhibiting large scale dynamics in all three dimensions while occupying a large volume of the phase space. From a global perspective, the dynamics of this LFF still connects the SLM to the HGR, however, fragmented into sections. Such dynamics is in stark contrast to the classical LFF trajectory of Fig. 2, where the laser occupies a minimum phase-space volume by following a rather ordered trajectory. An illustrative comparison of the dynamical evolution is provided by movies available online [15].

We further clarify the characteristic structure of the phase-space dynamics of fragmented LFFs by partitioning its phase-space trajectory. We concatenate data from the colored fragments in Fig. 3(a), and, in order to avoid including the transitions, neglect data located in a ~4 ns

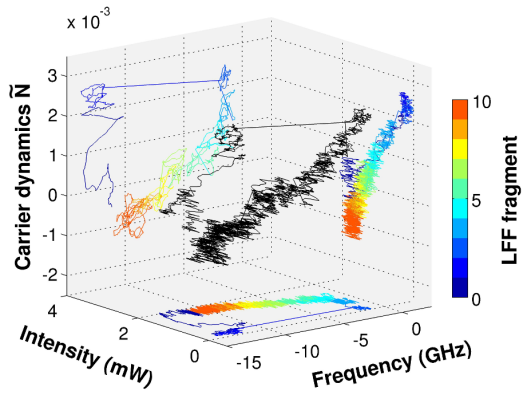

FIG. 4 (color online). Phase-space decomposition of the fragmented LFF. The shown dynamics results from concatenating the colored fragments in Fig. 3(a).

windows between individual fragments. Figure 4 shows the resulting phase-space trajectory of the concatenated data, with the discrete color bar indicating the number of delays elapsed after the initial dropout. To aid interpretation, the colors in Fig. 4 correspond to the color of fragments in Fig. 3(a). As the strong correspondence between Fig. 4 and Fig. 2(b) illustrates, for the concatenated data the laser exhibits dynamics resembling the conventional LFF. This demonstrates, first, the possibility to divide a delay laser's dynamical state into multiple fragments, and, second, the effective decoupling of these multiple fragments within the delay interval τ, as demonstrated by the robustness of the fragmentation. Such a long-lived fragmentation was recently identified in phase-clustered chimera states in complex networks [28–31]. In the state described here, both fragments exhibit disordered dynamics, while chimera states correspond to fragmentation into one ordered and one disordered fragment. Thus, the dissimilarity of dynamical characteristics is not fulfilled here, while the global fragmentation property appears comparable.

The large difference between the average intensity of the first and second fragments after the dropout, combined with the phase-space position of the first fragmentation event suggests injection locking as a mechanism. Locking of a laser to an injected optical field depends on the ratio between the injected and the local field. During a dropout, for a window of τ the laser's local field amplitude is significantly reduced, increasing the ratio between the injected and the local field and in turn exposes the laser to a state of increased susceptibility towards the delayed feedback. Simultaneously, the feedback contains high intensity pulses emitted from within the HGR where the laser resided one delay before. Therefore, the probability of injection locking the laser to its feedback signal depends on the feedback pulse statistics. The initial locking pulse experiences significant optical gain due to the strong increase in population inversion after the dropout. It therefore propagates through the delay system, relocking the laser to the HGR upon its return every τ. As a consequence, the injection locking event divides the laser's dynamical state into two fragments, which typically remain stable during one LFF cycle. Without the aid of phase-space tomography a correct identification of the mechanisms involved from experimental data would not have been possible.

Such fragmentation of dynamics occurring on the same attractor is only possible due to the introduced large separation between time scales. Relocking pulses are between 2 and 3 orders of magnitude shorter than the delay time τ, making the fragmentation process sensitive to the pulse statistics. We note that a fragmentation into more than two fragments is possible and has also been observed. In our experiments we find that conventional LFF cycles are not the dominant dynamical behavior under these experimental conditions. Sections with LFFs and fragmented LLFs appear to alternate irregularly, with the probability for fragmented LFFs decreasing with I_{bias}, from ~96% at $I_{\mathrm{bias}} = 7.65$ mA to ~79% at $I_{\mathrm{bias}} = 7.8$ mA. A reduction in feedback strength generally results in a fragmentation of the LFF cycle into more and more sections.

In conclusion, we demonstrate the simultaneous, temporally high-resolved characterization of the three physical phase-space variables intensity, frequency, and carrier inversion of a semiconductor laser. We therefore perform physically meaningful phase-space tomography of the system. Apart from the experimental illustration of conventional LFF phase-space trajectories, we identify a so far unreported modification to classical phase-space trajectories in the LFF regime and discuss the underlying physical mechanism. The association of the unconventional trajectories with injection locking motivates further theoretical analysis, even more since the dynamical state we report appears to be significant for delayed-feedback single mode semiconductor lasers in general [27].

From a general perspective, our experimental scheme represents a new technique to analyze semiconductor lasers. Applied to external-cavity laser systems, it opens new avenues for their stability analysis. The impact of stabilization schemes on phase, intensity, and population-inversion stability can be analyzed and optimized [32]. In injection-locked lasers, one can determine the full three-dimensional phase space [33]. Performing optimization of entire phase-space trajectories can decrease switching times in multistable systems [34,35], which could prove useful in multiple applications, for example, in telecommunication. Our scheme therefore presents an important step towards phase-space engineering [34,35] in semiconductor lasers.

Finally, an experimental determination of fundamental delay-attractor properties is still lacking. An example is the determination of Lyapunov exponents [36,37]. Providing access to additional physical dimensions of the system's state vector could allow for significantly improved

techniques and more reliable time series analysis and prediction [38]. Using state of the art realtime oscilloscopes would allow our scheme to measure optical spectra up to a width of 100 GHz in realtime. Such a broad spectral window enables the characterization of phase-space trajectories for the entire parameter range of such laser diodes, and therefore extend our approach to all relevant dynamical regimes.

This work was supported by Comunitat Autònoma de les Illes Balears via program Grups Competitius, FEDER and MINECO via project TRIPHOP (TEC2012-36335).

*d.brunner@ifisc.uib-csic.es

[1] R. F. Broom, Electron. Lett. **5**, 571 (1969).
[2] R. O. Miles, A. Dandridge, A. B. Tveten, T. G. Giallorenzi, and H. F. Taylor, Appl. Phys. Lett. **38**, 848 (1981).
[3] *International Spring School (Texel), The Netherlands 16–19 April 2000*, edited by B. Krauskopf and D. Lenstra (AIP, New York, 2000).
[4] D. Lenstra, B. Verbeek, and A. Den Boef, IEEE J. Quantum Electron. **21**, 674 (1985).
[5] I. Fischer, G. H. M. van Tartwijk, A. M. Levine, W. Elsäßer, E. Göbel, and D. Lenstra, Phys. Rev. Lett. **76**, 220 (1996).
[6] M. C. Soriano, J. Garcia-Ojalvo, C. R. Mirasso, and I. Fischer, Rev. Mod. Phys. **85**, 421 (2013).
[7] J. Ohtsubo, *Semiconductor Lasers: Stability, Instability and Chaos*, edited by W. T. Rhodes (Springer, Heidelberg, 2013).
[8] B. Tromborg and J. Mørk, IEEE J. Quantum Electron. **26**, 642 (1990).
[9] D. Brunner, X. Porte, M. C. Soriano, and I. Fischer, Sci. Rep. **2**, 732 (2012).
[10] F. Takens, *Dynamical Systems and Turbulence*, Lecture Notes in Mathematics, Vol. 898 (Springer-Verlag, Berlin, 1981), p. 366.
[11] B. Kelleher, D. Goulding, B. Baselga Pascual1, S. P. Hegarty, and G. Huyet, Eur. Phys. J. D **58**, 175 (2010).
[12] W. Ray, W. S. Lam, P. N. Guzdar, and R. Roy, Phys. Rev. E **73**, 026219 (2006).
[13] A. A. Sahai, B. Kim, D. Choi, A. Locquet, and D. S. Citrin, Opt. Lett. **39**, 5630 (2014).
[14] C. Risch and C. Voumard, J. Appl. Phys. **48**, 2083 (1977).
[15] See Supplemental Material at http://link.aps.org/supplemental/10.1103/PhysRevLett.115.053901, which includes Ref. [16], for technical details describing the procedure for extracting frequency and carrier dynamics from the recorded time traces.
[16] N. M. Al-Hosiny, I. D. Henning, and M. J. Adams, IEEE J. Quantum Electron. **42**, 570 (2006).
[17] I. Esquivias, S. Weisser, B. Romero, J. D. Ralston, and J. Rosenzweig, IEEE J. Quantum Electron. **35**, 635 (1999).
[18] K. Panajotov, M. Sciamanna, M. A. Arteaga, and H. Thienpont, IEEE J. Sel. Top. Quantum Electron. **19**, 1700312 (2013).
[19] T. Sano, Phys. Rev. A **50**, 2719 (1994).
[20] J. Zamora-Munt, C. Masoller, and J. García-Ojalvo, Phys. Rev. A **81**, 033820 (2010).
[21] R. Lang and K. Kobayashi, IEEE J. Quantum Electron. **16**, 347 (1980).
[22] X. Porte, M. C. Soriano, and I. Fischer, Phys. Rev. A **89**, 023822 (2014).
[23] J. Mørk, B. Tromborg, H. Sabbatier, and M. P. Sorensen, *IEEE Lasers and Electro-Optics Society, 1999 12th Annual Meeting* (IEEE, New York, 1999), Vol. 2, pp. 93–97.
[24] Y. Liu, P. Davis, and Y. Takiguchi, Phys. Rev. E **60**, 6595 (1999).
[25] J. Mørk, B. Tromborg, and P. L. Christiansen, IEEE J. Quantum Electron. **24**, 123 (1988).
[26] E. A. Viktorov, A. M. Yacomotti, and P. Mandel, J. Opt. B **6**, L9 (2004).
[27] L. Mashal, R. M. Nguimdo, G. Van der Sande, M. C. Soriano, J. Danckaert, and G. Verschaffelt, IEEE J. Quantum Electron. **49**, 790 (2013).
[28] D. M. Abrams and S. H. Strogatz, Phys. Rev. Lett. **93**, 174102 (2004).
[29] M. R. Tinsley, S. Nkomo, and K. Showalter, Nat. Phys. **8**, 662 (2012).
[30] A. M. Hagerstrom, T. E. Murphy, R. Roy, P. Hövel, I. Omelchenko, and E. Schll, Nat. Phys. **8**, 658 (2012).
[31] L. Larger, B. Penkovsky, and Y. Maistrenko, Phys. Rev. Lett. **111**, 054103 (2013).
[32] N. A. Loiko, A. V. Naumenko, S. I. Turovets, P. S. Spencer, and K. A. Shore, Quantum Semiclass. Opt. **9**, 853 (1997).
[33] S. Wieczorek, B. Krauskopf, T. B. Simpson, and D. Lenstra, Phys. Rep. **416**, 1 (2005).
[34] I. Z. Kiss, C. G. Rusin, H. Kori, and J. L. Hudson, Science **316**, 1886 (2007).
[35] M. Egerstedt, IEEE Trans. Autom. Control **51**, 110 (2006).
[36] J. D. Farmer, Physica (Amsterdam) **4D**, 366 (1982).
[37] R. Hegger, Phys. Rev. E **60**, 1563 (1999).
[38] M. Escalona-Moran, M. C. Soriano, J. Garcia-Prieto, I. Fischer, and C. R. Mirasso, Eur. Phys. J. Spec. Top. **223**, 2903 (2014).